

**Electronic band structure of a two-dimensional oxide quasicrystal**Cheng-Tien Chiang<sup>1,2</sup>, Martin Ellguth,<sup>2</sup> Florian O. Schumann,<sup>1</sup> Christian Tusche,<sup>2,3,4</sup> Richard Kraska,<sup>1</sup> Stefan Förster,<sup>1</sup> and Wolf Widdra<sup>1,2,\*</sup><sup>1</sup>*Institute of Physics, Martin-Luther-Universität Halle-Wittenberg, Von-Danckelmann-Platz 3, D-06120 Halle (Saale), Germany*<sup>2</sup>*Max-Planck-Institut für Mikrostrukturphysik, Weinberg 2, D-06120 Halle (Saale), Germany*<sup>3</sup>*Peter Grünberg Institut (PGI-6), Forschungszentrum Jülich, D-52425 Jülich, Germany*<sup>4</sup>*Fakultät für Physik, Universität Duisburg-Essen, D-47057 Duisburg, Germany* (Received 19 March 2019; revised manuscript received 30 August 2019; published 23 September 2019)

The valence band electronic structure of a BaTiO<sub>3</sub>-derived oxide quasicrystal (OQC) is studied by photoemission using momentum microscopy. An upward-dispersive O<sub>2p</sub> band is identified, and it can be assigned to a combination of in-plane orbitals according to the symmetry and the overlap of the wave functions. In addition, the signature of Ti<sub>3d</sub> states near the Fermi level is observed, which results in a metallic character of the OQC with 3d<sup>1</sup> occupation. Our experiments reveal two-dimensional electronic states within the OQC based on a symmetry-adapted decomposition of photoelectron intensity distribution in the momentum space.

DOI: [10.1103/PhysRevB.100.125149](https://doi.org/10.1103/PhysRevB.100.125149)**I. INTRODUCTION**

Since the discovery of quasicrystals (QCs), their special electronic structure has been a challenging topic [1]: The absence of translational symmetry prohibits the application of the Bloch theorem to describe their electronic states [2,3], which leads to a critical spatial extension of the wave functions [4–7]. In addition, dense Fourier components of the atomic potential from the aperiodic tiling can result in a large number of gaps in the electronic dispersion and cause a spiky density of states [8–12]. The dominant Fourier components also underlie the fascinating diffraction patterns, which have been recognized as one of the main characteristics of QCs.

In the pioneering works on metallic QCs with icosahedral and decagonal symmetry, the valence band electronic structure has been successfully visualized using angle-resolved photoelectron spectroscopy [13–17]. The corresponding quasicrystalline symmetry was observed in the energy-momentum dispersion  $E(\vec{k})$  of the free-electron-like  $sp$  bands. On the other hand, the role of orbital configurations as well as the role of the more localized  $d$  electrons have not been addressed so far. Recently, a novel class of QCs derived from BaTiO<sub>3</sub> and SrTiO<sub>3</sub> films with monolayer thickness has been discovered [18,19]. Studying the oxygen-derived valence bands in these oxide quasicrystals (OQCs) will provide a unique opportunity to reveal the impact of the orbital bonding geometry to  $E(\vec{k})$  in QCs, in contrast to the free-electron-like dispersion discussed so far. Due to the two-dimensional (2D) structure of the OQC, its  $E(\vec{k})$  can be characterized by the 2D momentum  $\vec{k} = (k_x, k_y)$  in the surface as provided intrinsically by valence-band photoemission with surface sensitivity.

In this paper, we report the 2D orbital character of O<sub>2p</sub> valence bands in the BaTiO<sub>3</sub>-derived dodecagonal OQC with their characteristic  $E(\vec{k})$  dispersion measured by momentum

microscopy [20]. A dispersive state with a unidirectional azimuthal ( $\phi$ ) intensity distribution extending up to 1 eV is clearly observed. This is in strong contrast to the less dispersive nonbonding O<sub>2p</sub> band and the O-Ti hybridized  $pd\pi$  state with their dominant isotropic and 2-fold  $\phi$ -dependent intensity. Our results directly demonstrate a close connection between the orbital configuration and the  $E(\vec{k})$  dispersion in QCs, which has not been established experimentally in previous literature due to the main focus on the free-electron-like bands and their folding. We demonstrate here that the occupation of Ti-3d states close to the Fermi level leads to a metallic character of the OQC, which explains the Ti<sup>3+</sup> character seen in x-ray photoelectron spectroscopy as well as the contrast mechanism in scanning tunneling microscopy [18].

The paper is organized as follows. The experimental setup and sample preparation are briefly described in Sec. II. Afterward, the results are presented and discussed in Sec. III, where the energy and momentum slices of photoelectron distribution are shown in Sec. III A. The photoelectron intensities are further decomposed into components according to their azimuthal angular distribution in Sec. III B, which reveals the dispersion of a specific O<sub>2p</sub> state of the OQC with an in-plane orbital character as discussed in Sec. III C. There, this  $2p_x$ - $2p_y$  state will be discussed in detail regarding its orbital character, dispersion relation, as well as the relevance of hybridization with the Pt substrate electronic structure. Thereafter, the signatures of Ti-3d states in the OQC will be discussed in Sec. III D and the role of the dodecagonal atomic potential in Sec. III E.

**II. EXPERIMENTS**

The OQCs were prepared by a dewetting-wetting process of ultrathin BaTiO<sub>3</sub> films on Pt(111) and checked by low energy electron diffraction (LEED) [18,21]. In Fig. 1 the LEED patterns on the OQC as prepared for the photoemission experiments are displayed, where the directions of the OQC

\*wolf.widdra@physik.uni-halle.de

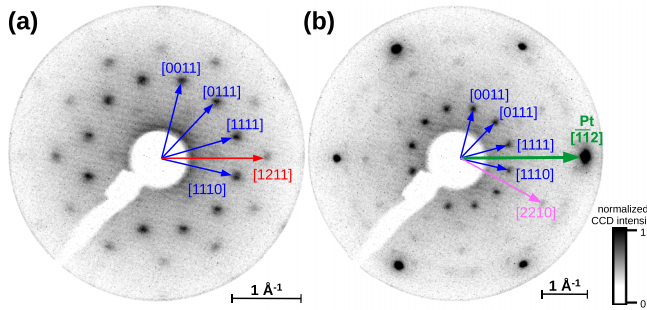


FIG. 1. Low energy electron diffraction (LEED) on the OQC at (a) 28 and (b) 66 eV. In both images the intensity is normalized to the [0011] spot of the OQC. In (a) the diffraction spot [1211] of the OQC is located at  $q_{[1211]} = 2k_r^{\text{kink}} \approx 1.5 \text{ \AA}^{-1}$ , which will be discussed later in Fig. 6 and Sec. III E 2. The [1111] spot as well as the [2210] spot in (b) are relevant for the possible umklapp processes and will be discussed in Sec. III E 1.

and Pt(111) are labeled by four and three indices, respectively. Special care had been taken to reduce the amount of the competing crystalline  $\text{BaTiO}_3(111)$  phase that was intentionally present in earlier work [18,21], and its photoemission data are provided in the Appendix A for comparison. The comprehensive maps of the photoelectron spectral function  $I(k_x, k_y, E_B)$  with the in-plane momentum components  $k_x, k_y$  and the binding energy  $E_B$  were recorded by the momentum microscope at 300 K with illumination of He-I radiation [20].

### III. RESULTS AND DISCUSSION

#### A. Overview of $k_x$ - $k_y$ and $E$ - $k_{x,y}$ maps

In Figs. 2 and 3 the 2D slices of the  $I(k_x, k_y, E_B)$  data sets of the OQC and the bare Pt(111) measured under identical conditions are shown. In the 2D momentum distribution in Fig. 2(a) for photoelectrons measured on OQC at the binding energy  $E_B = 0.5 \text{ eV}$ , dominant features of the Pt bulk bands from the underlying Pt substrate are observed as in Fig. 2(b) [23–26]. A closer inspection near the Pt  $\bar{M}$  point in the insets of Fig. 2(b) reveals the Pt surface resonance (SR) [23,25–27], which becomes suppressed in Fig. 2(a) due to the presence of the OQC. Similar observation also follows at the Fermi level ( $E_F$ ) as shown in Figs. 2(c), 2(d). Furthermore, on the OQC we observed a photoemission intensity asymmetry along the  $[\bar{1}12]$  high-symmetry direction of the underlying Pt(111) as shown in Fig. 3(a) ( $k_x$ ), whereas along the perpendicular direction  $k_y$  in Fig. 3(c) the intensity is distributed symmetrically. This observation can be attributed to the linear dichroism in the angular distribution of photoelectrons, which has been discussed thoroughly in the literature [28–30]. Comparing Figs. 3(a), 3(c) with the spectra on Pt in Figs. 3(b), 3(d) we can clearly identify the electronic states of the OQC at  $E_B = 4$  and 6 eV. These states are assigned to a nonbonding (NB) configuration of the oxygen  $2p$  orbitals and a  $\pi$ -bonding state between the Ti- $3d$  and O- $2p$  orbitals ( $pd\pi$ ) [22,31–33]. More importantly, a dispersive feature between the NB and the  $pd\pi$  states is observed as marked in Fig. 3(a).

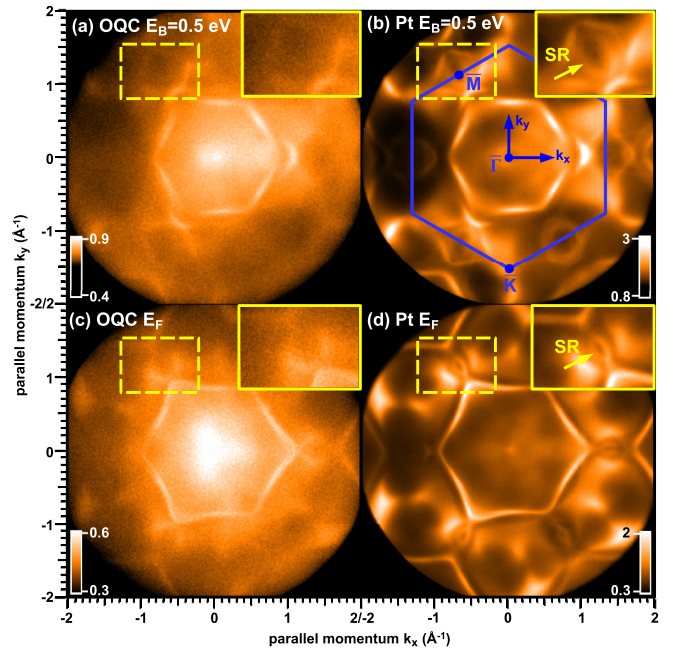


FIG. 2. 2D momentum maps of photoelectrons from (a), (c) the OQC and (b), (d) Pt(111). (a), (b) are measured at  $E_B = 0.5 \text{ eV}$ , and (c), (d) at the Fermi level ( $E_F$ ). The  $k_x, k_y$  directions and the surface Brillouin zone of Pt(111) are marked in (b) (blue). Insets: Magnified views near the Pt  $\bar{M}$  point (yellow), with Pt surface resonance (SR) in (b), (d). Color scale in  $10^4$  CCD counts.

#### B. Azimuthally decomposed photoemission intensity $I_n(k_r, E_B)$

To disentangle the dispersive electronic state in Fig. 3(a) from the less dispersive NB and  $pd\pi$  states, the photoemission intensity  $I(k_x, k_y, E_B)$  is decomposed into symmetry-adapted

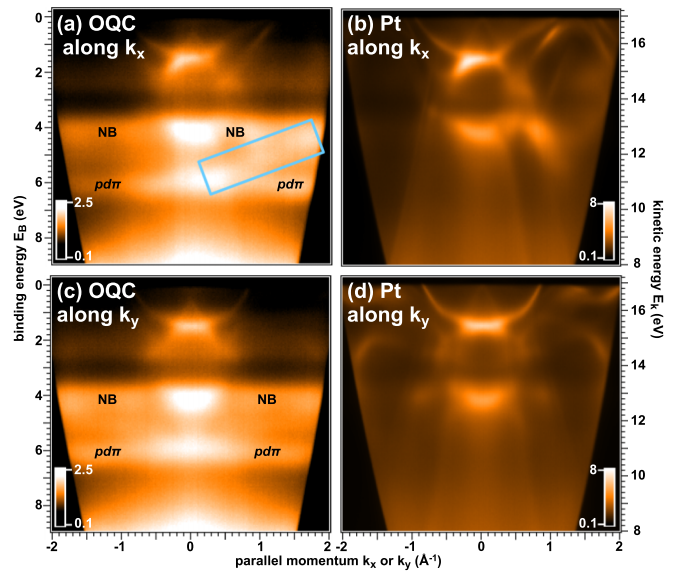


FIG. 3. Energy-momentum distribution of photoelectrons from (a), (c) the OQC and (b), (d) Pt(111). In (a) the dispersive oxygen-derived electronic state is marked. NB: Nonbonding O- $2p$  state;  $pd\pi$ :  $\pi$ -bonding state with Ti- $3d$  and O- $2p$  orbitals [22]. Color scale in  $10^4$  CCD counts.

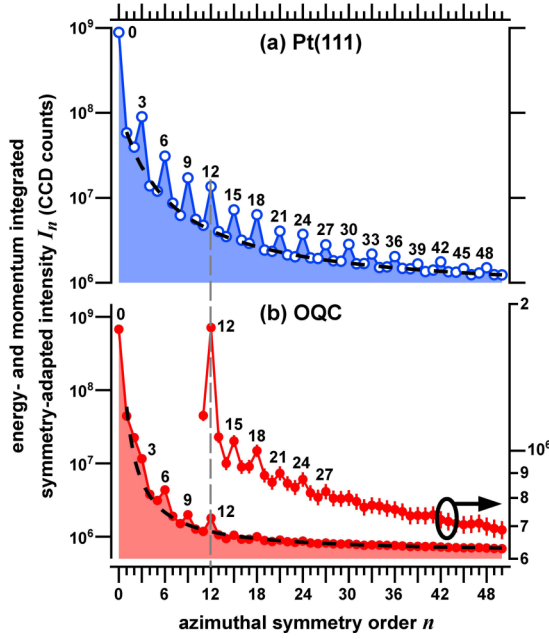


FIG. 4. Momentum- ( $k_r$ ) and energy- ( $E_B$ ) integrated symmetry-adapted photoemission intensity  $I_n(k_r, E_B)$  as a function of the azimuthal order  $n$  up to 50 for (a) Pt(111) and (b) the OQC. The numbers indicate clear oscillations with the multiples of the 3-fold symmetry at  $n = 3m$  orders, with  $m$  as an integer. Dashed curves are phenomenological fits with the function  $I_n = ae^{b/(n+c)}$  for the  $n \neq 3m$  orders. The fitting parameters are  $a_{\text{Pt}} = 6.9 \times 10^5$ ,  $b_{\text{Pt}} = 33$ ,  $c_{\text{Pt}} = 6.4$ , and  $a_{\text{OQC}} = 5.9 \times 10^5$ ,  $b_{\text{OQC}} = 9$ ,  $c_{\text{OQC}} = 0.95$ . Dashed vertical line marks  $n = 12$  as the expected first-order azimuthal symmetry of the OQC dodecagonal structure. In (b) the magnified view for  $n \geq 11$  is plotted with respect to the right vertical axis.

components  $I_n(k_r, E_B)$  by a Fourier series as

$$I(k_x, k_y, E_B) = \sum_{n=0}^{\infty} I_n(k_r, E_B) \cos(2\pi n\phi + \phi_0), \quad (1)$$

where the azimuthal angle ( $\phi$ ) and the magnitude of the parallel momentum ( $k_r$ ) are given by

$$\phi = \tan^{-1}(k_y/k_x) \quad (2)$$

and

$$k_r = \sqrt{k_x^2 + k_y^2}. \quad (3)$$

Our approach is similar to previous studies where the azimuthal ( $\phi$ ) angular distribution of photoelectrons is used to decompose the valence band spectra with element- and orbital-specificity [34,35]. The non-negative integer  $n$  describes the intensity variation along  $\phi$ , and  $\phi_0$  is an offset specified for each combination of  $n$ ,  $k_r$ , and  $E_B$ . In order to have an impression of the magnitude of  $I_n(k_r, E_B)$ , it is integrated over  $k_r$  and  $E_B$  and shown as a function of  $n$  for the Pt(111) in Fig. 4(a) and for the OQC in Fig. 4(b). As one can clearly see in Fig. 4(a), the  $k_r$ - and  $E_B$ -integrated  $I_n(k_r, E_B)$  of Pt(111) oscillates with a period of  $\Delta n = 3$  due to the 3-fold  $C_{3v}$  symmetry of the surface. For comparison, the oscillation in  $I_n$  is observed on the OQC in Fig. 4(b) only up to  $n \approx 24$ . As marked by the vertical dashed line in Fig. 4, on the Pt(111) and on the OQC there is about 0.97%

and 0.20% of the total photoemission intensity in the 12-fold component  $I_{12}$ , respectively. Since  $n = 12$  corresponds to the first-order azimuthal symmetry of the dodecagonal structure of the OQC, the energy and momentum dependence of  $I_{12}(k_r, E_B)$  will be discussed in more detail in Sec. III E. As shown by the semilogarithmic plots in Fig. 4, the intensities  $I_n(k_r, E_B)$  decrease rapidly as  $n$  increases. Therefore we focus only on the  $I_n(k_r, E_B)$  with  $n = 0$  to 12 as displayed in Fig. 5, whose sum contains 88% of all intensities for the OQC and 85% for the Pt(111). The estimation of systematic errors is presented in the Appendix B.

In Figs. 5(a)–5(c) and Figs. 5(h)–5(j) for the isotropic  $I_0$ , the unidirectional  $I_1$ , as well as the 2-fold  $I_2$  intensities, there are significant differences between the OQC and Pt. The unidirectional component  $I_1$  contains all features that are sensitive to the direction of the incident light and will be discussed in Sec. III C 2. In strong contrast to  $I_{0,1,2}$ , the spectra on the OQC with multiples of the 3-fold symmetry ( $I_{3,6,9,12}$ ) in Fig. 5 are similar to that of the Pt. Therefore, besides regions  $S_1$  to  $S_3$  in  $I_{12}$ , we ascribe the  $I_3$ ,  $I_6$ ,  $I_9$ , and  $I_{12}$  spectra of the OQC to photoelectrons from Pt transmitting directly through the ultrathin OQC layer. For example, the quenching of the Pt(111) surface resonance (SR) is visible in  $I_6$  at  $k_r = 1.3 \text{ \AA}^{-1}$  close to  $E_F$  when comparing Fig. 5(n) with Fig. 5(g). On the other hand, the dispersive state of the OQC can be clearly identified in  $I_1$  in Fig. 5(b) (rectangle) and unambiguously disentangled from the electronic states of the underlying Pt(111) in Fig. 5(i). Here we label this dispersive state of the OQC as  $2p_x$ - $2p_y$ , whose meaning will become clear later in the discussion.

### C. Dispersion and intensity of the $2p_x$ - $2p_y$ state

#### 1. Assignment to the $O_{2p}$ bands

To examine the dispersive  $2p_x$ - $2p_y$  state of the OQC more closely, the  $I_1(k_r, E_B)$  spectra of the OQC are displayed in Fig. 6(a) in detail. To quantitatively extract the dispersion of the  $2p_x$ - $2p_y$  state, the  $I_1(k_r, E_B)$  spectra are fitted at each individual  $k_r$ , as exemplarily shown in Fig. 6(b). The extracted peak positions of the  $2p_x$ - $2p_y$  state are summarized in Fig. 6(c), together with the observed NB and  $pd\pi$  states as well as the known oxygen  $2p$  ( $O_{2p}$ ) valence band regions in the literature [22,37,38] (R, W, E). In Fig. 6(c) the upward dispersion of the  $2p_x$ - $2p_y$  state can be clearly seen, which is located within the energy region of the  $O_{2p}$  valence bands of both crystalline and noncrystalline BaTiO<sub>3</sub> systems [22,37,38]. Therefore, the  $2p_x$ - $2p_y$  state is ascribed mainly to the  $O_{2p}$  orbitals.

Note that a similar upward dispersion has not been reported in any experimental work on periodic BaTiO<sub>3</sub> films [37,39,40]. In the theoretically calculated  $O_{2p}$  bands of various phases of BaTiO<sub>3</sub> [32,41–46], only one band disperses monotonically upward from the  $\Gamma$  point with the energy of the  $pd\pi$  bands toward the corners of the Brillouin zone, comparable to the observed  $2p_x$ - $2p_y$  state in Fig. 6(c). This upward-dispersive  $O_{2p}$  band consists of only pure  $O_{2p}$  orbitals along the  $\Gamma R$  and  $\Gamma M$  directions in the Brillouin zone [32,47]. Therefore, we assign the  $2p_x$ - $2p_y$  state of the OQC to a combination of mainly  $O_{2p}$  orbitals with a small hybridization of Ti-3d orbitals below 10% [48].

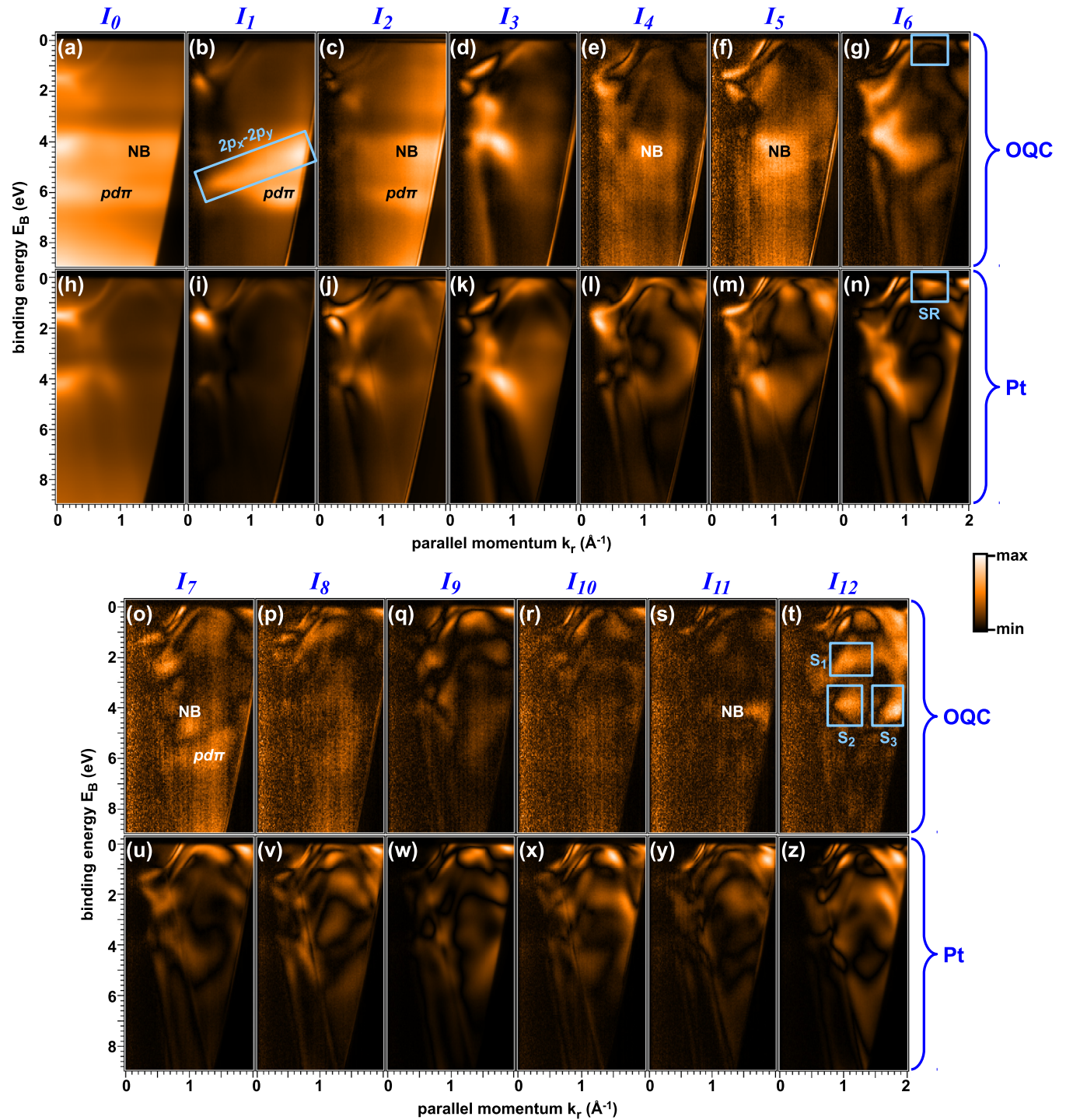


FIG. 5. Azimuthally decomposed photoemission intensity  $I_n(k_r, E_B)$  with  $n = 0$  to 12 of the OQC in (a)–(g) and (o)–(t), and Pt(111) in (h)–(n) and (u)–(z).  $2p_x-2p_y$ :  $O_{2p}$  state with combined orbitals in the surface plane. The minimum/maximum color scales are (a) 0.1/2.6, (b) 0/0.4, (c) 0/0.2, (d) 0/0.1, (e) 0/0.04, (f) 0/0.02, (g) 0/0.06, (h) 0.2/7.3, (i) 0/1.6, (j) 0/0.5, (k) 0/1.3, (l) 0/0.3, (m) 0/0.2, (n) 0/0.6, (o)–(p) 0/0.02, (q) 0/0.04, (r)–(t) 0/0.02, (u) 0/0.2, (v) 0/0.1, (w) 0/0.6, (x)–(y) 0/0.1, (z) 0/0.3 in  $10^4$  CCD counts. In (n), the label SR indicates the surface resonance of Pt(111) at  $\bar{M}$  points, which is quenched by the OQC in (g). In (t), the  $S_1$ ,  $S_2$ , and  $S_3$  indicate pronounced 12-fold features on the OQC.

## 2. Assignment to the combined in-plane $2p_x-2p_y$ orbitals

To understand the dispersion of the  $2p_x-2p_y$  state more quantitatively, the overlap between orbitals needs to be considered. The orbitals of the upward-dispersive  $O_{2p}$  band can

be estimated by a  $TiO_6$  cluster [32,49,50], which contains nearest-neighboring  $O_{2p}$  orbitals aligned either in parallel or perpendicular to each other. The latter, however, has a two times larger overlap between the orbitals than the former [32].

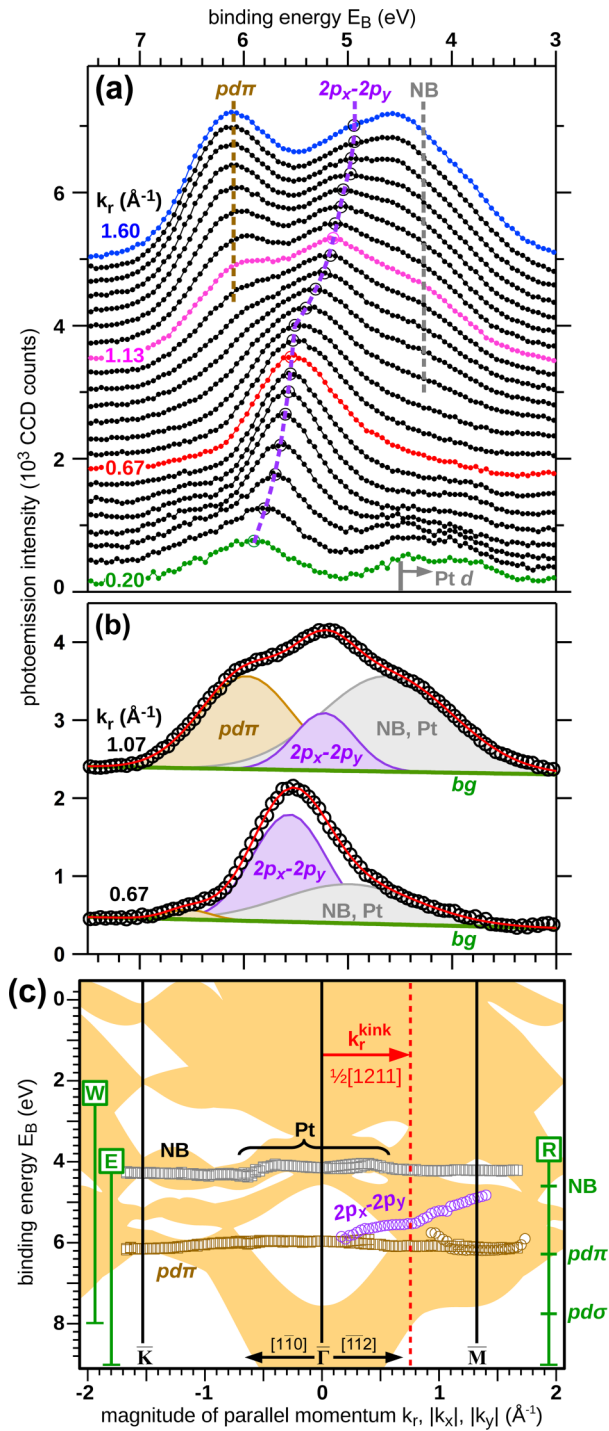


FIG. 6. (a)  $I_1(k_r, E_B)$  spectra with  $2p_x$ - $2p_y$ ,  $pd\pi$ , and NB states and the bottom of the bulk Pt- $d$  bands along  $\Lambda$  [36]. Dashed lines and circles are guides to the eye. (b) Two spectra from (a) fitted with three Gaussian functions for the  $pd\pi$  and the  $2p_x$ - $2p_y$  states, as well as the NB state with a possible contribution from Pt. Red curves are sums of the three peaks and a linear background (bg). Curves in (a) and (b) are shifted by 200 and 1700 CCD counts. (c)  $E(\vec{k})$  of  $O_{2p}$  bands. Circles:  $2p_x$ - $2p_y$  and  $pd\pi$  states in  $I_1(k_r, E_B)$ . Squares: NB and  $pd\pi$  states in Figs. 3(a) and 3(c). R, W, and E: Regions of  $O_{2p}$  bands and  $Ti_{3d}$ - $O_{2p}$   $pd\sigma$  bonding bands on BaTiO<sub>3</sub> crystals and films [22,37,38]. Pt: Bulk transitions in Pt [36]. Filled area: Surface-projected bands on Pt(111) [27].  $k_r^{\text{kink}}$  is related to the [1211] LEED spot in Fig. 1(a).

As a result, the transfer integral of the 90° orientated, nearest-neighboring  $O_{2p}$  orbitals amounts to 1.1 eV, which is 70% of the value in a  $\sigma$ -bonding geometry [32,51,52] and is larger than other combinations of  $O_{2p}$  orbitals along the Ti-O directions [32]. Because of this large transfer integral, the bandwidth of the  $2p_x$ - $2p_y$  state reaches 1 eV as shown in Fig. 6(c), and it is comparable to the  $O_{2p}$  bands in other bulk titanates and 2D oxygen structures [53–55].

The above assignment for the observed dispersive  $2p_x$ - $2p_y$  state as a combination of in-plane oxygen  $2p_x$  and  $2p_y$  orbitals can be more intuitively understood from two simplified perspectives: (1) The observed dispersion goes from a lower energy at the  $\bar{\Gamma}$  point toward higher energies (lower  $E_B$ ) at higher momenta. This upward dispersion cannot be derived from a band with only  $2p_x$  or  $2p_y$  orbitals because of their sign reversal in the orbital wave function. Instead, a  $2p_x$  band or a  $2p_y$  band has a downward dispersion from the  $\bar{\Gamma}$  point toward higher momenta along  $k_x$  or  $k_y$ , respectively [56,57]. (2) Neighboring  $2p_z$  orbitals perpendicular to the surface are in a  $\pi$ -bonding geometry and have much less overlap than most of the combinations of neighboring  $2p_x$  or  $2p_y$  orbitals. As a consequence, a band derived from the  $2p_z$  orbitals has the narrowest bandwidth among all  $O_{2p}$  valence bands [57,58] and cannot be responsible for the observed  $2p_x$ - $2p_y$  state.

The assignment of the  $2p_x$ - $2p_y$  state to the  $O_{2p}$  orbitals in the surface plane is further supported by the angular distribution of photoelectron intensity  $I_1$ . As shown in Fig. 5, the  $2p_x$ - $2p_y$  state is most clearly seen in the unidirectional intensity  $I_1$  in Fig. 5(b), whereas the NB and  $pd\pi$  states are mainly in the isotropic  $I_0$  and 2-fold  $I_2$  intensities. This observation is consistent with model calculations of photoemission [59,60], where an atomic  $p$  orbital oriented in the surface can yield a larger unidirectional intensity asymmetry than the  $p$  orbital perpendicular to the surface. Moreover, the clear dispersion of the  $2p_x$ - $2p_y$  state is evidence for the 2D delocalized electronic wave function in the OQC layer, in analogy to the dispersive  $O_{2p}$  bands for three-dimensional oxides [61]. This evidence is further supported by control experiments on BaTiO<sub>3</sub> islands (see Appendix A).

### 3. Possible hybridization with Pt electronic states

In Fig. 6(c) the surface-projected electronic band structure of Pt(111) is shown and several directional band gaps are displayed (white regions). Near the  $\bar{\Gamma}$  point, the  $2p_x$ - $2p_y$  state begins its upward dispersion at  $E_B \approx 6.0$  eV and is located within the energy-momentum region of a Pt(111) band gap extending from  $E_B = 4.6$  to 7.6 eV. Since electronic states within the band gap are forbidden in Pt(111), the  $2p_x$ - $2p_y$  state in the gap is confined within the OQC film and its wave function decays exponentially into the Pt substrate [62,63]. Because the dispersion of the  $2p_x$ - $2p_y$  state starts within the band gap of the Pt(111) surface where no Pt electrons are available, we exclude the hybridization with Pt electronic states or the interface state as the main origin of the observed dispersion. At the higher parallel momentum of  $k_r \approx 0.5 \text{ \AA}^{-1}$ , the dispersion of the  $2p_x$ - $2p_y$  state in Fig. 6(c) extends across the boundary of the Pt(111) band gap and enters into the energy-momentum regions of occupied Pt electronic states [27]. Consequently, at higher momenta with

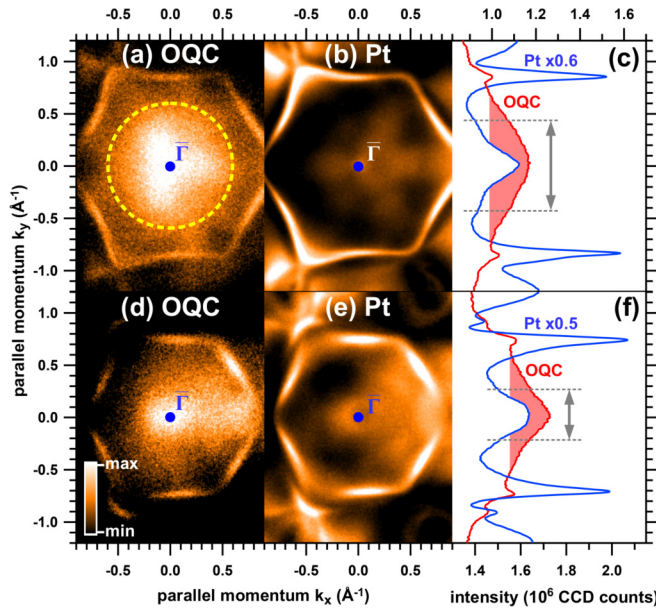


FIG. 7. 2D momentum map on (a), (d) the OQC and (b), (e) Pt(111), with (a), (b) at  $E_F$  and (d), (e) at  $E_B = 0.5$  eV. In (c), (f) their momentum distributions along  $k_y$ , integrated over  $k_x = \pm 0.5 \text{ \AA}^{-1}$  are shown, and the full width at half maximum near  $k_y = 0$  for OQC (filled regions) is estimated by the arrows. The minimum/maximum color scales are (a) 4.5/6, (b) 7/16, (d) 7.5/9, (e) 6/12, in  $10^3$  CCD counts. The Ti-3d<sup>1</sup> occupation in OQC is estimated by the circle in (a).

$k_r \geq 0.5 \text{ \AA}^{-1}$ , the overlap between the wave function of the  $2p_x-2p_y$  state and that of the Pt 5d and 6sp electrons can increase significantly and possible hybridization could occur.

#### D. Indication of the Ti-3d states

In addition to the  $O_{2p}$  bands, a closer look at the photoelectron momentum distribution near  $E_F$  in Fig. 7 reveals the occupation of the Ti-3d states within the OQC. As can be seen from the direct comparison between Fig. 7(a) and Fig. 7(b), additional spectral weight for the OQC is present around the  $\bar{\Gamma}$  point. This additional spectral weight can be better quantified in the momentum line profiles along  $k_y$  in Fig. 7(c), where the intensity on the OQC (red) is much higher at  $k_y = 0$  than at  $k_y \approx \pm 0.85 \text{ \AA}^{-1}$ , in opposition to the case of Pt(111) (blue). By assuming that the intensities at  $k_y \approx \pm 0.85 \text{ \AA}^{-1}$  completely result from Pt and the intensity ratio between the Pt features at  $k_y = 0$  and  $k_y \approx \pm 0.85 \text{ \AA}^{-1}$  is a constant, we can estimate the Pt contribution in the spectrum of the OQC in Fig. 7(a) at the  $\bar{\Gamma}$  point as 15%. Since 85% of the additional spectral weight at the  $\bar{\Gamma}$  point on the OQC is located in the energy and momentum region comparable to the occupied Ti-3d states in BaTiO<sub>3</sub> films doped by oxygen vacancies [39,40], we assign the observed additional spectral weight to the occupation of Ti-3d states.

At  $E_B = 0.5$  eV in Fig. 7(d) the intensity distribution on the OQC near the  $\bar{\Gamma}$  point becomes narrower than that at the  $E_F$  in Fig. 7(a), and it is comparable to that of the Pt(111) in Fig. 7(e). This can also be seen in the momentum profiles in

Fig. 7(f) and implies an  $E(\vec{k})$  dispersion of the Ti-3d states in the OQC. Due to the broad momentum distribution of photoelectrons from OQC near  $E_F$ , no clear  $E(\vec{k})$  dispersion could be identified for the Ti-3d states of the OQC. By assuming an upper bound of  $E_B = 0.5$  eV and a Fermi wave vector of  $0.6 \text{ \AA}^{-1}$ , a lower bound of the effective mass  $m_{\text{eff}} = 2.7m_e$  is estimated, with  $m_e$  as the rest mass of an electron. The dispersion of the Ti-3d states will be studied in the future using resonant photoemission.

The observed spectral weight of Ti-3d states is compatible with the assumption of a  $d^1$  configuration of each Ti atom within the OQC. From this assumption and from the area density of Ti atoms of  $2.5 \times 10^{14} \text{ cm}^{-2}$ , a corresponding Fermi wave vector of  $0.6 \text{ \AA}^{-1}$  follows and is indicated by the dashed circle in Fig. 7(a). The qualitative agreement for the observed photoemission intensity within the expected Fermi wave vector in Fig. 7(a) suggests a Ti-3d<sup>1</sup> configuration of the OQC. The 3d<sup>1</sup> configuration also explains straightforwardly the Ti<sup>3+</sup> signals from the earlier OQC samples in x-ray photoelectron spectroscopy [18], which were accompanied by the Ti<sup>4+</sup> signals of the remaining BaTiO<sub>3</sub>(111) islands from the final wetting process. From the 3d<sup>1</sup> configuration we expect a spin moment at each Ti site that might couple in a nontrivial way due to magnetic frustration within the aperiodic tiling [64,65]. The observation of a continuous density of states below  $E_F$  indicates the metallic character of the OQC, which suggests an alternative driving force other than the Hume-Rothery mechanism for the formation of the OQC [6,66–70].

### E. Role of the quasicrystal atomic potential

#### 1. Umklapp processes for photoelectrons from Pt

Last but not least, we discuss the possible influence of the quasicrystalline atomic potential to the observed  $E(\vec{k})$  and the photoemission process. As displayed in Fig. 5, the dominant photoemission features of the OQC are observed in  $I_0$ ,  $I_1$ , and  $I_2$ . Although the 12-fold intensity  $I_{12}$  in Fig. 5(t) has the same dodecagonal symmetry as the LEED pattern of the OQC [18,71], its magnitude is 20 times smaller than  $I_1$ . Furthermore, only the features  $S_1$  to  $S_3$  in  $I_{12}$  may be attributed to the OQC when comparing Fig. 5(t) with the data of Pt(111) in Fig. 5(z). As will be discussed in the following, we attribute the regions  $S_{1,2,3}$  at  $(k_r, E_B) = (1.1 \text{ \AA}^{-1}, 2.2 \text{ eV})$ ,  $(1.1 \text{ \AA}^{-1}, 3.9 \text{ eV})$ , and  $(1.9 \text{ \AA}^{-1}, 4.1 \text{ eV})$  to umklapp processes of photoelectrons coming from the Pt substrate being scattered by the OQC structure. For photoelectrons from Pt in Fig. 5(h) near  $E_B = 2.2$  eV, there is a broad feature at around  $(k_r, E_B) = (0.5 \text{ \AA}^{-1}, 2.3 \text{ eV})$ , and its momentum difference  $\Delta k_r$  from that of the  $S_1$  region is  $\Delta k_r \approx 0.6 \text{ \AA}^{-1}$ . This momentum difference could be provided by the umklapp process at the OQC with its theoretical position of the first-order LEED spot at  $q_{[0010]} = 0.52 \text{ \AA}^{-1}$ , which has been observed in our earlier LEED measurements at a much lower kinetic energy of 8 eV [18].

The regions  $S_2$  and  $S_3$  in Fig. 5(t) are located in the binding energy range near the intense photoemission feature of Pt at

$(k_r, E_B) = (0 \text{ \AA}^{-1}, 4.1 \text{ eV})$  in Fig. 5(h), with a difference in the momentum coordinate of  $\Delta k_r = 1.1 \text{ \AA}^{-1}$  for  $S_2$  and  $\Delta k_r = 1.9 \text{ \AA}^{-1}$  for  $S_3$ . The former value agrees with the position of the more intense [1111] LEED spot of the OQC in Fig. 1(b). The latter  $\Delta k_r = 1.9 \text{ \AA}^{-1}$  for  $S_3$  is comparable to the weaker [2210] LEED spot at  $q_{[2210]} = 2.0 \text{ \AA}^{-1}$  as also observed in Fig. 1(b). Therefore we attribute  $S_2$  and  $S_3$  to photoelectrons from the underlying Pt substrate undergoing umklapp processes with  $q_{[1111]}$  and  $q_{[2210]}$ , respectively.

## 2. Kink in the dispersion of the $2p_x-2p_y$ state

In addition to umklapp processes at the dodecagonal structure, a kink in the dispersion of the  $2p_x-2p_y$  state in Fig. 6(c) at  $k_r^{\text{kink}}$  is visible. Its position matches the expected momentum for a QC gap due to the  $q_{[1211]}$  Bragg peak:  $2k_r^{\text{kink}} = q_{[1211]} \approx 1.5 \text{ \AA}^{-1}$  in Fig. 1(a) [18,71,72]. Similarly to the formation of band gaps at the zone boundaries of periodic systems, the Fourier components of an aperiodic structure can lead to pseudogaps and folding of bands in the electronic dispersion  $E(\vec{k})$  [73,74]. In earlier photoemission model calculations for metallic QCs [73], the corresponding folding in  $E(\vec{k})$  can only be observed at strong Fourier components of the aperiodic potential. Therefore we attribute the absence of folded oxygen bands and pseudogaps in the dispersion in Fig. 6(c) to a weak influence of the QC atomic potential to the  $O_{2p}$  electrons, which is only sufficient to produce a kink in  $E(\vec{k})$ . Despite the more intense LEED spots at  $q_{[1111]}$  than  $q_{[1211]}$  in Fig. 1(a), the kink is only observed at  $0.5q_{[1211]}$ . This observation can be explained by the very different energy of the electrons in the diffraction process with a kinetic energy of 28 eV, which is about 36 eV higher than the  $O_{2p}$  valence bands at  $E_B = 4$  to 6 eV. As a consequence, the matrix element for the quasicrystal atomic potential is different for the wave function of the oxygen orbitals as compared to that for the electrons in the LEED process.

The indication of a weak influence from the quasicrystal potential to the  $O_{2p}$  electrons is further supported by the spatial extension of the  $O_{2p}$  wave function. The  $O^{2-}$  ion has an ionic radius of  $r_{O^{2-}} \approx 1.4 \text{ \AA}$  [75] and the  $O_{2p}$  orbital has an average radius of  $0.9 \text{ \AA}$  [76]. These values are much smaller than the next-neighbor Ti distance of  $a_{\text{OQC}} = 6.85 \text{ \AA}$  that provides the 12-fold potential in the OQC [18]. Moreover, the

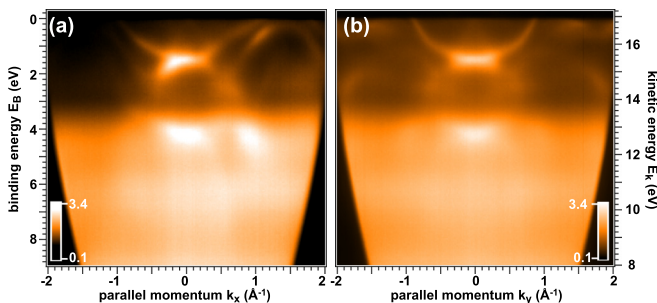


FIG. 8. Energy-momentum distribution of photoelectrons from periodic  $\text{BaTiO}_3(111)$  islands on  $\text{Pt}(111)$  for comparison with Fig. 3. Color scales are in  $10^4$  CCD counts.

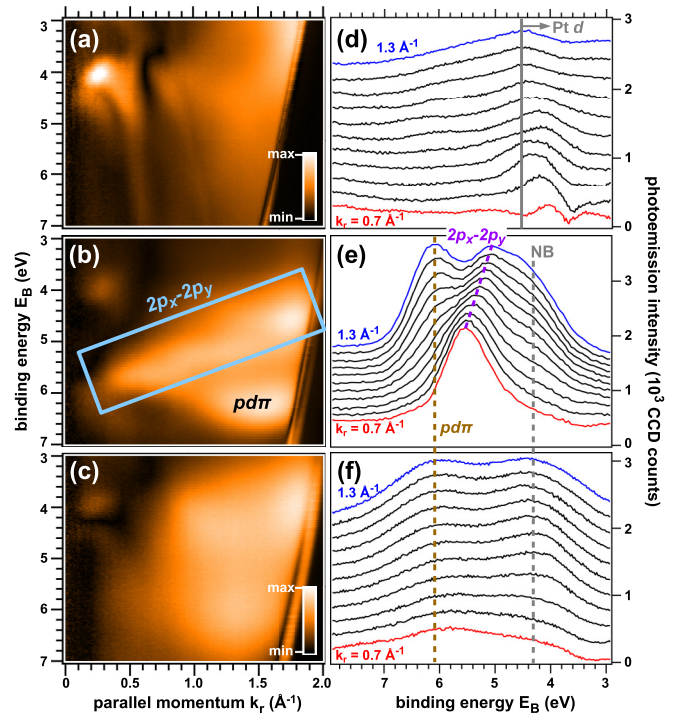


FIG. 9. Azimuthally decomposed photoemission intensity  $I_1(k_r, E_B)$  of (a)  $\text{Pt}(111)$ , (b)  $\text{BaTiO}_3$ -derived oxide quasicrystal (OQC), and (c)  $\text{BaTiO}_3(111)$  islands on  $\text{Pt}(111)$ . The line profiles of  $I_1(k_r, E_B)$  from (a), (b), and (c) at  $k_r = 0.7$  to  $1.3 \text{ \AA}^{-1}$  are shown in (d), (e), and (f), respectively. The minimum/maximum color scales in (a) and (c) are  $0/1.6$  and  $0/1.3 \times 10^3$  CCD counts. The color scale for (b) is the same as in Fig. 5(b). For clarity, curves in (d)–(f) are shifted vertically.

radial wave function of the  $O_{2p}$  orbital decreases from  $0.5 \text{ \AA}^{-1}$  to  $0.04 \text{ \AA}^{-1}$  when going from the radial distance of  $r_{O^{2-}}$  to  $a_{\text{OQC}}/2$  [77,78]. This reduction in the wave function by a factor of 10 at an increasing distance would lead to a decrease in the matrix element and the overlap integral between two  $O_{2p}$  orbitals by two orders of magnitude. As a result, the dispersion of the  $O_{2p}$  bands and the corresponding photoemission intensity is less influenced by the 12-fold long-range QC potential as compared to the delocalized free-electron-like states in metallic QCs [14,17,79].

## IV. SUMMARY

To summarize, the orbital configuration of the  $O_{2p}$  valence bands in the 2D  $\text{BaTiO}_3$ -derived oxide quasicrystal (OQC) is resolved by photoemission using momentum microscopy. We observe a clear upward energy-momentum dispersion of the  $2p_x-2p_y$  state with a kink associated with the diffraction spot at  $q_{[1211]}$  of the OQC, which suggests a weak interaction with the quasicrystal potential and might be a hint for a pseudogap. In the angular distribution of the photoelectrons, a 12-fold component can be identified. However, its magnitude is orders of magnitude lower than the lower symmetry components and it is tentatively attributed to umklapp scattering at the 12-fold quasicrystal potential. In addition, occupied Ti-3d states are

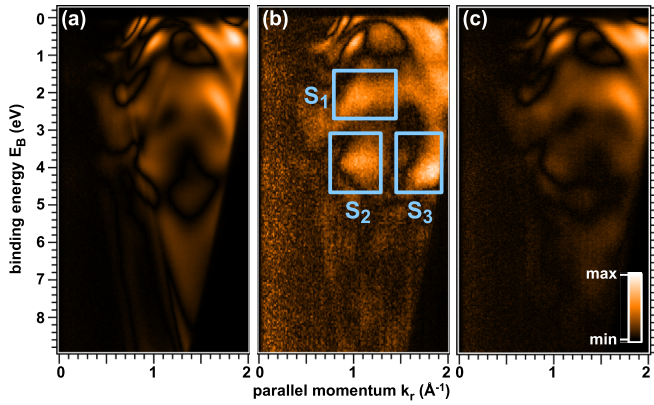


FIG. 10. Azimuthally decomposed photoemission intensity  $I_{12}(k_r, E_B)$  of (a) Pt(111), (b) the BaTiO<sub>3</sub>-derived OQC, and (c) BaTiO<sub>3</sub>(111) islands on Pt(111). Features  $S_{1,2,3}$  of the OQC in (b) are marked as in Fig. 5(t). The color scales for (a), (b) are the same as in Figs. 5(z), 5(t) and for (c) the minimum/maximum scales are  $0/5 \times 10^2$  CCD counts.

observed at  $E_F$  that lead to a metallic character of the BaTiO<sub>3</sub>-derived OQC.

#### ACKNOWLEDGMENTS

Technical support from F. Thiele and R. Kulla as well as fruitful discussion with S. Schenk and K.-M. Schindler are gratefully acknowledged. This work is partially funded by the Deutsche Forschungsgemeinschaft via SFB 762 (A3, B8).

#### APPENDIX A: COMPARISON BETWEEN THE OXIDE QUASICRYSTAL AND THE BaTiO<sub>3</sub>(111) ISLANDS

To support the dispersive  $2p_x$ - $2p_y$  state as a delocalized electronic state extended over the 2D BaTiO<sub>3</sub>-derived oxide quasicrystal (OQC), we compare in Figs. 8, 9, and 10 photoemission spectra measured on the OQC, the bare Pt(111), and the periodic BaTiO<sub>3</sub>(111) islands grown on Pt(111) by dewetting in oxygen atmosphere [21]. The raw data of the energy-momentum distribution from the BaTiO<sub>3</sub>(111) islands are shown in Fig. 8 for comparison with the data of the OQC and Pt in Fig. 3. In Fig. 8, mainly the dispersive features of Pt(111) are observed, together with the less dispersive features of the oxygen  $O_{2p}$  valence states at  $E_B \approx 4$  and 6 eV. As can be clearly seen in the unidirectional intensity  $I_1(k_r, E_B)$  in Figs. 9(b), 9(e) for the OQC in comparison with Figs. 9(c), 9(f) for the islands, the dispersive  $2p_x$ - $2p_y$  state is absent on the BaTiO<sub>3</sub>(111) islands. Instead, on the islands we

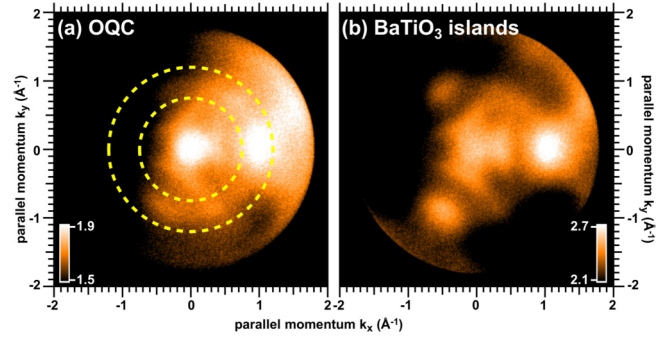


FIG. 11. 2D momentum distribution of photoelectrons from (a) the OQC and (b) the BaTiO<sub>3</sub> islands on Pt(111) at the binding energy  $E_B = 5.0$  eV. Color scales are in  $10^4$  CCD counts. Dashed circles in (a) enclose the region for the  $2p_x$ - $2p_y$  state.

observe in Fig. 9(f) less dispersive states at energies close to the oxygen  $pd\pi$  and nonbonding (NB) valence states. These  $O_{2p}$  states are consistent with the observation in Fig. 8.

In addition, the 12-fold intensity  $I_{12}(k_r, E_B)$  from the BaTiO<sub>3</sub>(111) islands in Fig. 10(c) is comparable to that of the Pt(111) in Fig. 10(a), but different from that of the OQC in Fig. 10(b). This observation reveals the influence of the OQC 2D atomic potential on the transmission of photoelectrons from the underlying Pt(111), resulting in features  $S_1$  to  $S_3$  in Fig. 10(b). Examples of the 2D momentum photoelectron distributions are shown in Fig. 11 for the OQC and the BaTiO<sub>3</sub>(111) islands at the binding energy  $E_B = 5.0$  eV. The area between the dashed circles in Fig. 11(a) is the region of the  $2p_x$ - $2p_y$  state. The intense 3-fold features in Fig. 11(b), which are also partially visible in Fig. 11(a), originate from Pt(111).

#### APPENDIX B: ESTIMATION OF SYSTEMATIC ERRORS IN $I_n(k_r, E_B)$

The intensity uncertainty of each of the  $I_n(k_r, E_B)$  can be estimated by their square root values according to the Poisson statistics, which is less than 15% for the  $S_1$  to  $S_3$  regions in the  $I_{12}(k_r, E_B)$  of the OQC in Fig. 5(t) as well as most of the visible regions in the  $I_{12}(k_r, E_B)$  of the Pt(111) in Fig. 5(z). Another systematic error is introduced by the uncertainty in determining the origin of the  $k_x$ - $k_y$  plane, which enters Eq. (1) by the definition of the  $k_r$ . In our experiments the origin of the  $k_x$ - $k_y$  plane can be determined more precisely than  $1 \times 10^{-2} \text{ \AA}^{-1}$  in the presence of an instrumental resolution better than  $5 \times 10^{-3} \text{ \AA}^{-1}$  [20], and the resultant relative error is less than 10% for the momentum regions with  $k_r \geq 0.1 \text{ \AA}^{-1}$ .

- [1] D. Shechtman, I. Blech, D. Gratias, and J. W. Cahn, Metallic Phase with Long-Range Orientational Order and No Translational Symmetry, *Phys. Rev. Lett.* **53**, 1951 (1984).  
 [2] M. Kohmoto, L. P. Kadanoff, and C. Tang, Localization Problem in One Dimension: Mapping and Escape, *Phys. Rev. Lett.* **50**, 1870 (1983).

- [3] S. Ostlund, R. Pandit, D. Rand, H. J. Schellnhuber, and E. D. Siggia, One-Dimensional Schrödinger Equation with an Almost Periodic Potential, *Phys. Rev. Lett.* **50**, 1873 (1983).  
 [4] L. C. Collins, T. G. Witte, R. Silverman, D. B. Green, and K. K. Gomes, Imaging quasiperiodic electronic states in a synthetic Penrose tiling, *Nat. Commun.* **8**, 15961 (2017).

- [5] T. Fujiwara and T. Yokokawa, Universal Pseudogap at Fermi Energy in Quasicrystals, *Phys. Rev. Lett.* **66**, 333 (1991).
- [6] A. P. Smith and N. W. Ashcroft, Pseudopotentials and Quasicrystals, *Phys. Rev. Lett.* **59**, 1365 (1987).
- [7] M. Kohmoto, B. Sutherland, and C. Tang, Critical wave functions and a Cantor-set spectrum of a one-dimensional quasicrystal model, *Phys. Rev. B* **35**, 1020 (1987).
- [8] J. Nayak, M. Maniraj, A. Rai, S. Singh, P. Rajput, A. Gloskovskii, J. Zegenhagen, D. L. Schlagel, T. A. Lograsso, K. Horn, and S. R. Barman, Bulk Electronic Structure of Quasicrystals, *Phys. Rev. Lett.* **109**, 216403 (2012).
- [9] R. Widmer, P. Gröning, M. Feuerbacher, and O. Gröning, Experimental signatures of spiky local density of states in quasicrystals, *Phys. Rev. B* **79**, 104202 (2009).
- [10] Z. M. Stadnik, D. Purdie, Y. Baer, and T. A. Lograsso, Absence of fine structure in the photoemission spectrum of the icosahedral Al-Pd-Mn quasicrystal, *Phys. Rev. B* **64**, 214202 (2001).
- [11] E. S. Zijlstra and T. Janssen, Non-spiky density of states of an icosahedral quasicrystal, *Europhys. Lett.* **52**, 578 (2000).
- [12] Z. M. Stadnik, D. Purdie, M. Garnier, Y. Baer, A.-P. Tsai, A. Inoue, K. Edagawa, S. Takeuchi, and K. H. J. Buschow, Electronic structure of quasicrystals studied by ultrahigh-energy-resolution photoemission spectroscopy, *Phys. Rev. B* **55**, 10938 (1997).
- [13] X. Wu, S. W. Kycia, C. G. Olson, P. J. Benning, A. I. Goldman, and D. W. Lynch, Electronic Band Dispersion and Pseudogap in Quasicrystals: Angular-Resolved Photoemission Studies on Icosahedral Al<sub>70</sub>Pd<sub>21.5</sub>Mn<sub>8.5</sub>, *Phys. Rev. Lett.* **75**, 4540 (1995).
- [14] E. Rotenberg, W. Theis, K. Horn, and P. Gille, Quasicrystalline valence bands in decagonal AlNiCo, *Nature (London)* **406**, 602 (2000).
- [15] W. Theis, E. Rotenberg, K. J. Franke, P. Gille, and K. Horn, Electronic valence bands in decagonal Al-Ni-Co, *Phys. Rev. B* **68**, 104205 (2003).
- [16] E. Rotenberg, W. Theis, and K. Horn, Electronic structure investigations of quasicrystals, *Prog. Surf. Sci.* **75**, 237 (2004).
- [17] V. A. Rogalev, O. Gröning, R. Widmer, J. H. Dil, F. Bisti, L. L. Lev, T. Schmitt, and V. N. Strocov, Fermi states and anisotropy of Brillouin zone scattering in the decagonal Al-Ni-Co quasicrystal, *Nat. Commun.* **6**, 8607 (2015).
- [18] S. Förster, K. Meinel, R. Hammer, M. Trautmann, and W. Widdra, Quasicrystalline structure formation in a classical crystalline thin-film system, *Nature (London)* **502**, 215 (2013).
- [19] S. Schenk, S. Förster, K. Meinel, R. Hammer, B. Leibundgut, M. Paleschke, J. Pantzer, C. Dresler, F. O. Schumann, and W. Widdra, Observation of a dodecagonal oxide quasicrystal and its complex approximant in the SrTiO<sub>3</sub>-Pt(111) system, *J. Phys.: Condens. Matter* **29**, 134002 (2017).
- [20] C. Tusche, A. Krasnyuk, and J. Kirschner, Spin resolved bandstructure imaging with a high resolution momentum microscope, *Ultramicroscopy* **159**, 520 (2015).
- [21] S. Förster, J. I. Flege, E. M. Zollner, F. O. Schumann, R. Hammer, A. Bayat, K.-M. Schindler, J. Falta, and W. Widdra, Growth and decay of a two-dimensional oxide quasicrystal: High-temperature in situ microscopy, *Ann. Phys.* **529**, 1600250 (2017).
- [22] S. Robey, L. Hudson, V. Henrich, C. Eylem, and B. Eichhorn, Resonant photoelectron spectroscopy studies of BaTiO<sub>3</sub> and related mixed oxides, *J. Phys. Chem. Solids* **57**, 1385 (1996).
- [23] W. Di, K. E. Smith, and S. D. Kevan, Angle-resolved photoemission study of the clean and hydrogen-covered Pt(111) surface, *Phys. Rev. B* **45**, 3652 (1992).
- [24] E. Frantzeskakis, S. Pons, A. Crepaldi, H. Brune, K. Kern, and M. Grioni, Ag-coverage-dependent symmetry of the electronic states of the Pt(111)-Ag-Bi interface: The ARPES view of a structural transition, *Phys. Rev. B* **84**, 245443 (2011).
- [25] H. Herrera-Suárez, A. Rubio-Ponce, and D. Olgún, Electronic band structure of the Pt(111) surface: An *ab initio* and tight-binding study. I, *Comput. Mater. Sci.* **56**, 141 (2012).
- [26] Y. S. Kim, S. H. Jeon, A. Bostwick, E. Rotenberg, P. N. Ross, A. L. Walter, Y. J. Chang, V. R. Stamenkovic, N. M. Markovic, T. W. Noh, S. Han, and B. S. Mun, Role of preferential weak hybridization between the surface-state of a metal and the oxygen atom in the chemical adsorption mechanism, *Phys. Chem. Chem. Phys.* **15**, 19019 (2013).
- [27] A. D. Corso, Clean Ir(111) and Pt(111) electronic surface states: A first-principles fully relativistic investigation, *Surf. Sci.* **637-638**, 106 (2015).
- [28] S. Chernov, K. Medjanik, C. Tusche, D. Kutnyakhov, S. Nepijko, A. Oelsner, J. Braun, J. Minár, S. Borek, H. Ebert, H. Elmers, J. Kirschner, and G. Schönhense, Anomalous *d*-like surface resonances on Mo(110) analyzed by time-of-flight momentum microscopy, *Ultramicroscopy* **159**, 453 (2015).
- [29] C. Tusche, P. Goslawski, D. Kutnyakhov, M. Ellguth, K. Medjanik, H. J. Elmers, S. Chernov, R. Wallauer, D. Engel, A. Jankowiak, and G. Schönhense, Multi-MHz time-of-flight electronic bandstructure imaging of graphene on Ir(111), *Appl. Phys. Lett.* **108**, 261602 (2016).
- [30] Y. Ishida, H. Kanto, A. Kikkawa, Y. Taguchi, Y. Ito, Y. Ota, K. Okazaki, W. Malaeb, M. Mulazzi, M. Okawa, S. Watanabe, C.-T. Chen, M. Kim, C. Bell, Y. Kozuka, H. Y. Hwang, Y. Tokura, and S. Shin, Common Origin of the Circular-Dichroism Pattern in Angle-Resolved Photoemission Spectroscopy of SrTiO<sub>3</sub> and Cu<sub>x</sub>Bi<sub>2</sub>Se<sub>3</sub>, *Phys. Rev. Lett.* **107**, 077601 (2011).
- [31] R. E. Cohen and H. Krakauer, Electronic structure studies of the differences in ferroelectric behavior of BaTiO<sub>3</sub> and PbTiO<sub>3</sub>, *Ferroelectrics* **136**, 65 (1992).
- [32] P. Pertosa and F. M. Michel-Calendini, X-ray photoelectron spectra, theoretical band structures, and densities of states for BaTiO<sub>3</sub> and KNbO<sub>3</sub>, *Phys. Rev. B* **17**, 2011 (1978).
- [33] Ş. Ellialtıođlu and T. Wolfram, Surface electronic properties of *d*-band perovskites: Study of the  $\pi$  bands, *Phys. Rev. B* **18**, 4509 (1978).
- [34] A. Stuck, J. Osterwalder, T. Greber, S. Hüfner, and L. Schlapbach, Partial Densities of States of Alloys Measured with X-Ray-Photoelectron Diffraction: AuCu<sub>3</sub>(001), *Phys. Rev. Lett.* **65**, 3029 (1990).
- [35] C. Søndergaard, C. Schultz, M. Schønning, S. Lizzit, A. Baraldi, S. Agergaard, M. B. Nielsen, H. Li, and P. Hofmann, Symmetry-resolved density of states from valence band photoelectron diffraction, *Phys. Rev. B* **64**, 245110 (2001).
- [36] E. Tamura, W. Piepke, and R. Feder, Spin-resolved photoemission from (111) surfaces of Pd, Ir, and Pt by circularly polarised light: Theory and comparison with experiment, *J. Phys.: Condens. Matter* **1**, 6469 (1989).

- [37] J. L. Wang, A. Pancotti, P. Jégou, G. Niu, B. Gautier, Y. Y. Mi, L. Tortech, S. Yin, B. Vilquin, and N. Barrett, Ferroelectricity in a quasicrystalline ultrathin BaTiO<sub>3</sub> film, *Phys. Rev. B* **84**, 205426 (2011).
- [38] D. Ehre, H. Cohen, V. Lyahovitskaya, and I. Lubomirsky, X-ray photoelectron spectroscopy of amorphous and quasicrystalline phases of BaTiO<sub>3</sub> and SrTiO<sub>3</sub>, *Phys. Rev. B* **77**, 184106 (2008).
- [39] S. Muff, N. Pilet, M. Fanciulli, A. P. Weber, C. Wessler, Z. Ristić, Z. Wang, N. C. Plumb, M. Radović, and J. H. Dil, Influence of ferroelectric order on the surface electronic structure of BaTiO<sub>3</sub> films studied by photoemission spectroscopy, *Phys. Rev. B* **98**, 045132 (2018).
- [40] P. Lutz, S. Moser, V. Jovic, Y. J. Chang, R. J. Koch, S. Ulstrup, J. S. Oh, L. Moreschini, S. Fatale, M. Grioni, C. Jozwiak, A. Bostwick, E. Rotenberg, H. Bentmann, and F. Reinert, Volatile two-dimensional electron gas in ultrathin BaTiO<sub>3</sub> films, *Phys. Rev. Mater.* **2**, 094411 (2018).
- [41] Q.-J. Liu, N.-C. Zhang, F.-S. Liu, H.-Y. Wang, and Z.-T. Liu, BaTiO<sub>3</sub>: Energy, geometrical and electronic structure, relationship between optical constant and density from first-principles calculations, *Opt. Mater.* **35**, 2629 (2013).
- [42] S. Sanna, C. Thierfelder, S. Wippermann, T. P. Sinha, and W. G. Schmidt, Barium titanate ground- and excited-state properties from first-principles calculations, *Phys. Rev. B* **83**, 054112 (2011).
- [43] A. Koleżyński and K. Tkacz-Śmiech, From the molecular picture to the band structure of cubic and tetragonal barium titanate, *Ferroelectrics* **314**, 123 (2005).
- [44] M. Veithen, X. Gonze, and P. Ghosez, Electron localization: Band-by-band decomposition and application to oxides, *Phys. Rev. B* **66**, 235113 (2002).
- [45] S. Saha, T. P. Sinha, and A. Mookerjee, Electronic structure, chemical bonding, and optical properties of paraelectric BaTiO<sub>3</sub>, *Phys. Rev. B* **62**, 8828 (2000).
- [46] P. Ghosez, X. Gonze, and J. P. Michenaud, First-principles characterization of the four phases of barium titanate, *Ferroelectrics* **220**, 1 (1999).
- [47] The symmetry of the oxygen bands can be found in Table I of Refs. [50,52].
- [48] R. E. Cohen, Origin of ferroelectricity in perovskite oxides, *Nature (London)* **358**, 136 (1992).
- [49] T. Wolfram, R. Hurst, and F. J. Morin, Cluster surface states for TiO<sub>2</sub>, SrTiO<sub>3</sub>, and BaTiO<sub>3</sub>, *Phys. Rev. B* **15**, 1151 (1977).
- [50] A. H. Kahn and A. J. Leyendecker, Electronic energy bands in strontium titanate, *Phys. Rev.* **135**, A1321 (1964).
- [51] F. M. Michel-Calendini and G. Mesnard, Band structure and optical properties of tetragonal BaTiO<sub>3</sub>, *J. Phys. C: Solid State Phys.* **6**, 1709 (1973).
- [52] L. F. Mattheiss, Band structure and Fermi surface of ReO<sub>3</sub>, *Phys. Rev.* **181**, 987 (1969).
- [53] Y. Haruyama, S. Kodaira, Y. Aiura, H. Bando, Y. Nishihara, T. Maruyama, Y. Sakisaka, and H. Kato, Angle-resolved photoemission study of SrTiO<sub>3</sub> (100) and (110) surfaces, *Phys. Rev. B* **53**, 8032 (1996).
- [54] M. Takizawa, K. Maekawa, H. Wadati, T. Yoshida, A. Fujimori, H. Kumigashira, and M. Oshima, Angle-resolved photoemission study of Nb-doped SrTiO<sub>3</sub>, *Phys. Rev. B* **79**, 113103 (2009).
- [55] W. Eberhardt and F. J. Himpsel, Dispersion and Symmetry of Oxygen-Induced Bands on Al(111), *Phys. Rev. Lett.* **42**, 1375 (1979).
- [56] J. C. Slater and G. F. Koster, Simplified LCAO method for the periodic potential problem, *Phys. Rev.* **94**, 1498 (1954).
- [57] R. Hoffmann, How chemistry and physics meet in the solid state, *Angew. Chem., Int. Ed. Engl.* **26**, 846 (1987).
- [58] I. P. Batra and S. Ciraci, Electronic Structure of the Oxygen Overlayer on Al(100), *Phys. Rev. Lett.* **39**, 774 (1977).
- [59] M. Greif, L. Castiglioni, A. P. Seitsonen, S. Roth, J. Osterwalder, and M. Hengsberger, Photoelectron diffraction in the x-ray and ultraviolet regime: Sn-phthalocyanine on Ag(111), *Phys. Rev. B* **87**, 085429 (2013).
- [60] J. W. Gadzuk, Surface molecules and chemisorption. II. Photoemission angular distributions, *Phys. Rev. B* **10**, 5030 (1974).
- [61] N. Barrett, J. E. Rault, J. L. Wang, C. Mathieu, A. Locatelli, T. O. Mendes, M. A. Niño, S. Fusil, M. Bibes, A. Barthélémy, D. Sando, W. Ren, S. Prosandeev, L. Bellaiche, B. Vilquin, A. Petraru, I. P. Krug, and C. M. Schneider, Full field electron spectromicroscopy applied to ferroelectric materials, *J. Appl. Phys.* **113**, 187217 (2013).
- [62] F. Forstmann, The concepts of surface states, *Prog. Surf. Sci.* **42**, 21 (1993).
- [63] N. Memmel, Monitoring and modifying properties of metal surfaces by electronic surface states, *Surf. Sci. Rep.* **32**, 91 (1998).
- [64] A. I. Goldman, Magnetism in icosahedral quasicrystals: Current status and open questions, *Sci. Technol. Adv. Mater.* **15**, 044801 (2014).
- [65] D. Shi, Z. Budrikis, A. Stein, S. A. Morley, P. D. Olmsted, G. Burnell, and C. H. Marrows, Frustration and thermalization in an artificial magnetic quasicrystal, *Nat. Phys.* **14**, 309 (2018).
- [66] J. Friedel, Do metallic quasicrystals and associated Frank and Kasper phases follow the Hume Rothery rules? *Helv. Phys. Acta* **61**, 538 (1988).
- [67] R. D. Werkman, P. J. Schurer, I. Vincze, and F. van der Woude, Are quasicrystals Hume-Rothery alloys? *Hyperfine Interact.* **45**, 409 (1989).
- [68] G. T. de Laissardière, D. Mayou, and D. N. Manh, Electronic structure of transition atoms in quasi-crystals and Hume-Rothery alloys, *Europhys. Lett.* **21**, 25 (1993).
- [69] A.-P. Tsai, A test of Hume-Rothery rules for stable quasicrystals, *J. Non-Cryst. Solids* **334-335**, 317 (2004).
- [70] U. Mizutani, T. Takeuchi, and H. Sato, Interpretation of the Hume-Rothery rule in complex electron compounds:  $\gamma$ -phase Cu<sub>5</sub>Zn<sub>8</sub> alloy, FK-type Al<sub>30</sub>Mg<sub>40</sub>Zn<sub>30</sub> and MI-type Al<sub>68</sub>Cu<sub>7</sub>Ru<sub>17</sub>Si<sub>8</sub>1/1 - 1/1 - 1/1 approximants, *Prog. Mater. Sci.* **49**, 227 (2004).
- [71] N. Niizeki and H. Mitani, Two-dimensional dodecagonal quasilattices, *J. Phys. A: Math. Gen.* **20**, L405 (1987).
- [72] The theoretical position is at  $q_{[1211]} = 1.44 \text{ \AA}^{-1}$  as a third-order [1211] diffraction spot from the Ti and Ba lattice.
- [73] E. Rotenberg, W. Theis, and K. Horn, Model simulations of momentum-resolved photoemission from quasicrystals, *J. Alloys Compd.* **342**, 348 (2002).
- [74] J. Voit, L. Perfetti, F. Zwick, H. Berger, G. Margaritondo, G. Grüner, H. Höchst, and M. Grioni, Electronic structure of solids with competing periodic potentials, *Science* **290**, 501 (2000).

- [75] R. D. Shannon, Revised effective ionic radii and systematic studies of interatomic distances in halides and chalcogenides, *Acta Crystallogr., Sect. A* **32**, 751 (1976).
- [76] G. Burns and E. G. Wikner, Antishielding and contracted wave functions, *Phys. Rev.* **121**, 155 (1961).
- [77] R. E. Watson, Analytic Hartree-Fock solutions for  $O^=$ , *Phys. Rev.* **111**, 1108 (1958).
- [78] J. Redinger and K. Schwarz, Electronic charge distribution of the polarizable  $O^{2-}$  ion in MgO and CaO in contrast to the  $F^-$  ion in NaF, *Z. Phys. B: Condens. Matter* **40**, 269 (1981).
- [79] S. J. Ahn, P. Moon, T.-H. Kim, H.-W. Kim, H.-C. Shin, E. H. Kim, H. W. Cha, S.-J. Kahng, P. Kim, M. Koshino, Y.-W. Son, C.-W. Yang, and J. R. Ahn, Dirac electrons in a dodecagonal graphene quasicrystal, *Science* **361**, 782 (2018).